1 **MESOPOROUS NiO/Al-SBA-15 CATALYSTS FOR SOLVENT-FREE**

2 **DEOXYGENATION OF PALM FATTY ACID DISTILLATE**

3 Khairul Basyar Baharudin[a,b*], Taufik Yap Yun Hin[c], James Hunns,[d] Mark Isaacs,[e] Karen

4 Wilson,[d] Darfizzi Derawi[a*]

5 [a]Advanced Oleochemicals and Sustainable Bioenergy Laboratory, Center for Advanced

6 Materials and Renewable Resources, Faculty of Science and Technology, Universiti

7 Kebangsaan Malaysia, 43600 UKM Bangi, Selangor, Malaysia

8 [b]Faculty of Biotechnology and Biomolecular Science, University Putra Malaysia,

9 43400 UPM Serdang, Selangor, Malaysia

10 [c]Department of Chemistry, Faculty of Science, Universiti Putra Malaysia,

11 43400 UPM Serdang, Selangor, Malaysia

12 [d]Applied Chemistry and Environmental Science, School of Science,

13 RMIT University, 124 La Trobe Street, Melbourne, Victoria 3000, Australia,

14 [e]Department of Chemistry, University College London, Gower Street, London, UK, WC1E

15 6BT

16 *CORRESPONDING AUTHOR**

17 darfizzi@ukm.edu.my, basyar@upm.edu.my

18

ABSTRACT

A series of 5 wt% NiO/Al-SBA-15 catalysts were prepared by wet impregnation of ordered, mesoporous Al-SBA-15 supports (Si/Al molar ratios spanning 5-75) synthesised by a true liquid crystal templating (TLCT) method. The catalytic activity of the resulting catalysts was studied in the solventless, hydrogen-free deoxygenation (DO) of palm fatty acid distillate (PFAD), using a semi-batch reactor at 350 °C. ^{27}Al and ^{29}Si MAS-NMR was used to quantify the speciation of framework and extra-framework Al as a function of Si:Al ratio, before and after NiO functionalisation; TEM and XRD confirmed the formation of 9-10 nm NiO nanoparticles in all cases. NiO/Al-SBA-15 catalysts exhibited excellent catalytic activity for PFAD deoxygenation, with hydrocarbon yields reaching 86 % and a selectivity to the diesel fraction (C_{11}-C_{17}) of 91 %.

1. INTRODUCTION

Research and development into the production of green diesel fuel from renewable plant, algae or fatty acid containing oil feedstocks is an attractive advanced technology to replace the use of fossil fuels as transportation fuels, and reduce the worldwide dependence on crude oil as a main energy source. Green diesel can be classified as a second-generation biofuel as it involves the use of non-food derived resources as the feedstock, such as lignocellulosic waste biomass, waste cooking oil and non-edible components of plant material [1–5].

42   Palm oil is among the most traded vegetable oil in the world, and approximately 90%

43   of the world's palm oil exports are produced in Asia, mostly in Malaysia and Indonesia.

44   Studies on converting biomass from the palm oil industry to green diesel are at an early stage,

45   however methods to reduce the cost of raw materials has emerged as a priority to improve

46   the economic viability of green diesel as a fuel [6,7]. Numerous types of low-grade oils and

47   waste biomass are produced by the palm oil industry that are suitable for conversion to green

48   diesel, the most notable of which is palm fatty acid distillate (PFAD). Use of low value

49   PFAD, which is a common by-product or waste from the palm oil refining process, as a

50   feedstock has potential to reduce the cost of green diesel production, while also eliminating

51   environmental pollution associated with current problems of improper disposal of PFAD into

52   water ways. PFAD typically comprises > 80% free fatty acid (FFA), mostly palmitic, stearic,

53   oleic, and linoleic acids, along with a small percentage of lauric, myristic and linolenic acids.

54   Glycerides, vitamin E, squalene, sterols and volatile substances are also present as minor

55   components of PFAD [8–10]. The high percentage of FFA makes PFAD a highly promising

56   potential feedstock for green diesel production.

57   Deoxygenation (DO) and hydrodeoxygenation (HDO) are well-known technologies

58   for green diesel production. Both processes produce green diesel which is less-oxygenated

59   with high oxidative stability and properties similar to those of conventional petroleum-

60   derived fuels [11–13]. HDO is an expensive route to product fuel, as the reaction requires

61   high pressures and high volumes of H_2 gas to remove oxygen from FFA [15] as H_2O. In

62   contrast DO is more economical, and involves hydrocarbon chain cracking and removal of

63   oxygen from the FFA structure as CO_2/CO via decarboxylation/decarbonylation

64   (DCX/DCN) reactions [14,15]. For both reactions, catalyst design is very important to

65   promote optimum yields of straight hydrocarbons from PFAD (the reaction feedstock), and

66   can be controlled by tuning the physicochemical properties of catalysts. Particle size, particle

67   distribution and surface morphology, as well as the purity, must be controlled to obtain

68   catalysts with tailor-made chemical and physical properties suitable for particular

69   applications and specific reaction systems that give the desired final product [16,17].

70   Choosing the right catalyst support is crucial because the support can enhance the catalytic

71   activity by promoting active metal dispersion, increasing the number of active sites by

72   forming new active phases, stabilizing active phases, minimizing the effect of coke-induced

73   deactivation and decreasing the cost of the catalyst [14,16,18–20].

74   SBA-15 has received considerable attention as a templated mesoporous catalyst

75   support for heterogeneous catalysis because of its 2D hexagonal pore structure, controllable

76   pore diameter, narrow pore size distribution and large pore volume [21,24,25]. SBA-15 is

77   also readily modified to incorporate an active metal or promoter and tune activity for a

78   specific application, [26,27] with the incorporation of aluminium into the SBA-15 framework

79   one approach to introduce acid sites on the support [27–31]. Transition metals catalyst have

80   been extensively applied in numerous catalyst reaction systems, such as DO, HDO, oxidation

81   and reduction [32,33], with nickel of particular interest as an active phase owing to its low

82   cost and high earth abundance compared with noble metals [34–36]. Supported nickel

83   catalysts are however prone to deactivation by coking and sintering during HDO and DO

84   processes, however, the use of acidic supports are known to increase the interaction of nickel

85   with the support and improve catalytic activity [18]. The use of highly ordered

86   mesostructured acidic Al-SBA-15 materials should be attractive supports for DO catalysts as

87   their large specific surface areas facilitate high dispersions of active metal or metal oxide

88 particles [21], while the presence of large pore diameters should improve the diffusion and

89 adsorption of large FFA molecules at the active site [22,23].

90 Here, we report the preparation of a 5wt% NiO/Al-SBA-15 catalysts using a wet

91 impregnation process in which the acidic properties of the Al-SBA-15 catalyst support was

92 systematically tuned by varying the Si/Al molar ratio from 5-75. The Al-SBA-15 catalyst

93 support was prepared using the true liquid crystal template (TLCT) so as to achieve high

94 structural order in the mesoporous support [ref]. Resulting 5wt% NiO/Al-SBA-15 catalysts

95 are utilised in the production of hydrocarbon-based green diesel via solventless, hydrogen

96 free deoxygenation of palm fatty acid distillate.

97

98 **2. EXPERIMENTAL**

99 **2.1 Material**

100 Analytical grade reagents were used to synthesize catalysts in this work without

101 further purification. Pluronic P123 ((triblock copolymer poly(ethylene glycol)-

102 poly(propylene glycol)-poly(ethylene glycol) with an average molecular weight of 5800 was

103 purchased from Sigma-Aldrich, tetramethylorthosilicate (TMOS) ($C_4H_{12}O_4Si$) with purity $\geq$

104 98%, aluminium nitrate nonahydrate ($Al(NO_3)_3.(9H_2O)$) with > 99% purity and 2 M

105 hydrochloric acid (HCl) were obtained from Merck. Nickel (II) nitrate hexahydrate

106 ($Ni(NO_3)_2.6H_2O$) with > 99% purity was purchased from the R&M Company. Absolute

107 ethanol (C_2H_6O) was purchased from Fisher Scientific.

108 The PFAD used as a feedstock in this work was generously provided by the Catalysis

109 Science and Technology Research Centre (PutraCat), and was used as a starting material for

110 DO reactions without any pretreatments. PFADs were composed of high fractions (81.7%)

111   of FFAs and glycerides (14.4%) with trace amounts of vitamin E, squalene, sterol and other

112   volatile substances. Typically, the FFAs fraction of Malaysian PFAD is composed of

113   saturated fatty acids such as lauric acid (0.2%), myristic acid (1.2%), palmitic acid (47.1%)

114   and stearic acid (4.5%) and unsaturated fatty acids such as oleic acid (36.6%), linoleic acid

115   (9.6%) and linolenic acid (0.47%) [8,37].

116

117   **2.2 Catalyst Synthesis**

118   **2.3 Synthesis of Al-SBA-15 support**

119   Al-SBA-15 supports with different Si/Al molar ratios (5, 25, 50 and 75) were

120   prepared using the TLCT method. Pluronic P-123 (2g) and appropriate amount of

121      $Al(NO_3)_3.(9H_2O)$ were dissolved in acidified water, (pH 2 (HCl)) contained within a

122   polypropylene bottle. The mixture was subsequently immersed in an ultrasonic water bath at

123   40 °C for 2 hours to produce a homogenous gel, after which 4.08 ml of TMOS was added to

124   the stirred solution until a smooth gel with a free-flowing liquid was observed. Methanol

125   evolved in the reaction was removed under light vacuum (100 mbar) at 40 °C for 18 hours in

126   a vacuum oven. The resulting dried samples were ground into a fine powder and calcined in

127   a muffle furnace at a ramp rate of 1.5 °C min^{-1} to 550 °C, where it was maintained for 5 hours.

128

129   **2.4 Synthesis of Ni/Al-SBA-15**

130   The Ni/Al-SBA-15 catalyst was prepared using $(Ni(NO_3)_2.6H_2O)$ as the Ni precursor.

131   In this wet impregnation method, x g of $Ni(NO_3)_2.6H_2O$ (estimated to give a 5 wt.% Ni

132   loading) was dissolved into x ml ethanol under stirring. 1g of finely ground Al-SBA-15

133   powder was the added to the solution and continuously stirred vigorously at ambient

134   temperature for a few hours. Next, the solution was heated slowly with stirring at ~80 °C and

135   maintained until the light green milky suspension was almost dry. The resulting material was

136   dried for 18 hours in an electrical oven at 80 °C. The resulting dried samples were ground

137   into a fine powder and then calcined in a muffle furnace at ramp rate of 5 °C min^{-1} to 550 °C,

138   where it was maintained for 5 hours. The resulting catalysts were labelled NiO/Al-SBA-

139   15(n), where n denotes the Si/Al molar ratio (5, 25, 50 and 75). NiO/SBA-15 was also

140   prepared for comparison using the same procedure. The SBA-15 catalyst support was

141   prepared using the same TLCT method described in the literature[24].

142

143   **2.5 Catalyst Characterization**

144   The resulting powder samples were characterized using a Bruker D8 Advance

145   diffractometer fitted with a LynxEye X'celerator detector at CuKα (λ = 1.54 Å) for phase

146   confirmation. X-ray diffraction (XRD) patterns were collected by wide-angle scans between

147   10° to 80°, with a step size of 0.02° and a scan rate of 1 s. Low-angle XRD patterns were

148   scanned between 0.45 to 8°, with a step size of 0.01° and scan rate of 0.6 s. The Scherrer

149   equation was used to calculate the volume-averaged crystallite diameters. An ASAP

150   Micromeritics 2020 instrument was used to analyse the catalysts by N_2 physisorption. All

151   catalysts were degassed at 150 °C for two hours to remove moisture and unknown gases

152   before the nitrogen gas adsorption-desorption measurements were conducted at -196 °C. The

153   specific surface area was calculated by the Brunauer–Emmett–Teller (BET) method, and the

154   pore size distribution and pore volume of the catalyst were calculated by the Barrett-Joyner-

155   Halenda (BJH) method using the nitrogen desorption branches of the isotherm. An X-ray

156   fluorescence (XRF) (Bruker S8 Tiger) instrument equipped with a rhodium tube operating at

157 4 kW was used to determine the elemental composition and metal loading of the catalysts.

158 Samples were analysed without any special pre-treatment.

159 The acidity of the catalyst was investigated through temperature programmed

160 reaction of propylamine, using thermogravimetric analysis coupled with mass spectrometry

161 (TGA-MS). Prior to analysis, 30 mg of catalyst was wet-impregnated with a small amount

162 of propylamine (Sigma-Aldrich, $\geq$ 99%) and dried in a fume hood under lamellar flow before

163 drying in a vacuum oven overnight at 40°C. The impregnated catalyst was analysed by TGA

164 instrument (Mettler Toledo TGA/DSC2 STAR) between 40 and 800 °C under flowing

165 nitrogen (30 ml/min) at a ramp rate of 10 °C/min. The effluent gas from TGA was passed

166 and monitored through a Pfeiffer Vacuum ThermoStar MS at m/Z = 41 for propene

167 desorption. The acidity of the catalyst was measured by quantification of reactively formed

168 propene from the acid sites. The characteristic acid sites (Brønsted/Lewis) on the catalyst

169 were studied with a diffuse reflectance infrared Fourier transform spectroscopy (DRIFTS)

170 using pyridine as a probe molecule. Prior to analysis, the catalysts were ground with KBr (50

171 wt.%) into a fine powder, wetted with neat pyridine and left to dry under a fume hood before

172 drying overnight in a vacuum oven at 40 °C. DRIFT spectra were collected at room

173 temperature in absorbance mode using a Thermo scientific Nicolet iS50 FTIR spectrometer

174 with an MCT detector and Smart Collector accessory. Solid-state ^{27}Al and ^{29}Si nuclear

175 magnetic resonance (NMR) spectra were recorded at 104.20 MHz and 79.49 MHz,

176 respectively, using a Bruker Avance III HD spectrometer attached to a 4 mm magic-angle

177 spinning (MAS) probe. ^{27}Al spectra were obtained using direct excitation with a pulse angle

178 of approximately 30 degrees, with a 0.2 s recycle delay and a sample spin-rate of

179 approximately 14 kHz. ^{29}Si spectra were obtained using direct excitation with background

180   suppression with a 60 s recycle delay and a sample spin-rate of 8 kHz. Spectral referencing

181   was made with respect to an external sample of aqueous 1 M aluminium nitrate for ^{27}Al and

182   neat tetramethyl silane for ^{29}Si. The morphology of the resulting catalyst was examined using

183   high-resolution transmission electron microscopy (HRTEM, 200 kV FEI Tecnai F20 Super-

184   Twin) coupled to energy dispersive spectroscopy (EDS, Oxford Instrument X-Max^N 80T) for

185   element mapping and further determination of the elemental composition of the synthesized

186   catalyst.

187

188   2.6 Catalytic Deoxygenation of PFAD

189   The DO of PFAD was performed in semi-batch mode with a 250 ml three-necked

190   flask reactor in a heating mantle equipped with a modified reflux distillation unit and nitrogen

191   gas flow in a combined system. Approximately 5 wt. % loading of supported NiO catalyst

192   was added to PFAD without liquid solvent in the reactor. Before the reaction started, nitrogen

193   was flowed through the reactor system to ensure the reaction occurred in the inert

194   atmosphere. Under constant stirring and with a nitrogen flow rate of approximately 20

195   cc/min, the temperature was increased to the desired temperature of 350 °C and maintained

196   for 2 hours. During the DO reaction, nitrogen gas carried all evolved gases/vapours to the

197   cooled condenser, in which condensable (deoxygenated) products can be collected at the

198   vessel collector, while nitrogen gas continues to flow to a trap containing 50 ml of 1 M

199   sodium hydroxide. The external circulating cooling water was used to ensure that the

200   condenser temperature was below 15 °C. After the reaction was completed, the reactor

201   temperature was decreased to room temperature, and the nitrogen flow was stopped.

202

203 **2.7 Diesel Composition Analysis**

204　　　　The final liquid phase of the DO fraction products was analysed by gas

205　chromatography (GC, Agilent 7890A Series) equipped with an HP-5 capillary column

206　(length: 30 m × inner diameter: 0.32 mm × film thickness: 0.25 µm) and flame ionization

207　detector (FID). A series of alkane and alkene standards (C_8-C_{20}), and 1-bromohexane as an

208　internal standard was acquired from Sigma-Aldrich, and employed for identification and

209　quantitative analysis. GC-grade n-hexane was used to dilute the resulting liquid product prior

210　to yield analysis, with an aliquot of approximately 1 µl was injected into the GC column. The

211　column inlet temperature and FID detector were set to 250 °C and 300 °C, respectively. The

212　oven temperature was held for 6 min at 40 °C and increased to 270 °C at a heating rate of 7

213　°C/min.

214　　　　The performance of the catalyst in the DO process with PFAD was evaluated by the

215　percentage of both saturated and unsaturated straight-chain hydrocarbon yields (X). All

216　analyses were repeated several times with the same condition to validate the reliability of the

217　results.

218
$$X = \frac{\sum na + \sum nb}{\sum nz} \times 100\%$$

219　where: na = area of alkene (C_8-C_{20}), nb = area of alkane (C_8-C_{20}), and nz = area of product

220

221　　　　The hydrocarbon selectivity (Y) of the hydrocarbon was calculated by:

222
$$Y = \frac{Cx}{\sum nx} \times 100\%$$

223　where: Cx = area of desired hydrocarbon fraction, and nx = area of hydrocarbon

224

3. RESULTS AND DISCUSSION

3.1 Physicochemical Properties of the Catalyst

Low-angle and wide-angle XRD patterns of both the catalyst support and corresponding supported NiO catalysts are illustrated in **Figures 1** and S**1**. The parent Al-SBA-15 all show well defined low angle diffraction peaks ~1.1-1.2° indicative of the (100) reflection of the hexagonal porous network (**Figure S1a**), while wide angle patterns show no evidence of crystalline phases of Al_2O_3, suggesting the successful incorporation of Al^{3+} into the silica framework (**Figure S1b**). Following impregnation with NiO, low angle XRD (**Figure 1a**) demonstrates the two-dimensional *p6mm* hexagonal arrangement of the Al-SBA-15 and SBA-15 supports were retained, however, a slight decrease in the (100) and (110) reflections, suggests a slight decrease in the mesopore ordering in the final supported NiO catalyst [30,36,38]. The good crystallinity and phase purity of NiO is shown in the wide-angle XRD pattern in **Figure 1b**. The observed broad peak at ~20°-30° for all synthesized catalysts (**Figures S1b and 1b)** was attributed to amorphous silica in the framework. The effective impregnation of NiO on both Al-SBA-15 and SBA-15 catalyst supports, can be verified the presence of diffraction peaks at ~37.22°, 43.19°, and 62.74°, which correspond to the (111), (200) and (220) planes of face-centred cubic NiO (JCPDS 01-075-0197). No other peaks related to unknown phases were visible (within the detection limits of XRD), indicating that the condition used in this synthesis could produce a relatively pure phase of supported NiO on Al-SBA-15 and SBA-15.

245   All synthesized SBA-15 and Al-SBA-15 materials in **Figure S2a** exhibit similar Type

246   IV isotherms, consistent with purely mesoporous materials with similar pore sizes and non-

247   intersecting mesopores [40,41]. Impregnation with NiO (**Figure 2a**) does not change the

248   mesoporous structure of the catalysts, which retain the structural characteristics typical of

249   TLCT synthesized SBA-15 [24]. All NiO/SBA-15 and NiO/Al-SBA-15 catalysts exhibit the

250   H1 hysteresis loop attributed to a honeycomb-like mesoporous structure with well-defined

251   cylindrical pore channels [42]. Slight differences in magnitude of the hysteresis, particularly

252   for NiO/Al-SBA-15(25), may reflect the decreased pore diameter, which falls into a regime

253   where a significant hysteresis loop is not expected [ref]. The existence of Al^{3+} in the matrix

254   of mesoporous $Al-SiO_2$ catalyst supports has previously been observed to alter the pore and

255   textural properties relative to pure SiO_2 supports [12,43]. **Figures S2b** and **2b** show narrow

256   pore size distributions for all synthesized catalyst supports and corresponding supported NiO

257   catalysts, confirming the genesis of highly dispersed NiO nanoparticles does not disrupt the

258   porous hexagonal structure of the support.

259   **Table 1**, summarises the physicochemical properties of the parent supports and NiO

260   doped catalysts. SBA-15 has the largest specific surface area (698 m^2g^{-1}) with the specific

261   surface area decreasing as more Al^{3+} is incorporated into the SBA-15 framework. The

262   variation of surface area with Al^{3+} content is shown in **Figure S3**, for the lowest concentration

263   of Al^{3+} (Si/Al = 75) the surface area decreases to 410 m^2g^{-1}, then remains constant at 386

264   m^2g^{-1} and 384 m^2g^{-1} respectively for Si/Al = 25 and 50, before decreasing to 309 m^2g^{-1} for

265   the highest concentration of Al^{3+} (Si/Al = 5). A similar trend, albeit with lower surface area,

266   is observed upon introduction of NiO into the Al/SBA-15 and SBA-15 catalyst supports.

267   This decrease in surface area is associated with the deposition of NiO, including particle

268   aggregation of the synthesized material during calcination, which may partially blocked some

269   pores or cover the surface catalyst of the SBA-15, affecting the silica network connectivity

270   contributing to a decrease in surface area [39][6].

271

272   **TABLE 1**. Physicochemical properties of the synthesized catalysts

Catalyst	BET surface area (m^{2}g^{-1})	Pore volume^a (cm^{3}g^{-1})	Average Pore size^b (nm)	NiO Crystallite size^c (nm)	Ni content[d] (wt.%)	Si/Al molar ratio[d]	Acid site loading[e] (mmolg^{-1})
SBA-15	698	0.978	6.2	-	-	-	-
NiO-SBA-15	522	0.924	6.9	9.7 ± 0.5	7.10	-	0.144
Al-SBA-15(75)	410	0.402	3.4	-	-	113.49	0.215
NiO/Al-SBA 15(75)	264	0.305	3.6	9.7 ± 0.5	7.16	61.07	0.219
Al-SBA-15(50)	384	0.420	4.5	-	-	69.50	0.231
NiO/Al-SBA-15(50)	254	0.342	4.2	9.8 ± 0.5	7.35	41.07	0.242
Al-SBA-A-	386	0.322	3.2	-	-	38.20	0.297

15(25)							
NiO/Al-SBA-15(25)	261	0.247	3.1	9.4 ± 0.5	6.82	24.85	0.322
Al-SBA-15(5)	309	0.360	3.6	-	-	7.75	0.486
NiO/Al-SBA-15(5)	164	0.193	3.4	9.6 ± 0.5	6.42	5.39	0.500

a. BJH desorption pore volume
b. BJH desorption average pore diameter
c. Calculated using the Scherrer equation based on the XRD diffraction pattern
d. Estimated from the XRF analysis (errors in Si/Al = ± 20%)
e. Calculated by propylamine TGA-MS analysis

The pore volume of SBA-15 was highest at 0.978 cm^3/g, consistent with the highest surface area, whereas the NiO/Al-SBA-15(5) catalyst exhibited the lowest pore volume, 0.193 cm^3/g and surface area. The incorporation of Al^{3+} into the SBA-15 framework had a significantly reduced the pore volume, with further reduction observed upon subsequent doping with NiO. The SBA-15 support and NiO-SBA-15 catalyst have slightly higher average pore sizes of ~6-7 nm, while Al-SBA-15 samples possessed smaller average pore size of ~3.2-4.5 nm which were largely unchanged upon incorporation of NiO. The estimated average crystallite size of NiO of NiO-SBA-15 and all NiO/Al-SBA-15 catalysts were determined to be ~9-10 nm according to the Debye Scherer method (**Table 1**). These were

288   obviously larger than the average pore size of the catalyst support, indicating that a number

289   of NiO particles were present on the external surface of the mesoporous catalyst support.

290   The elemental composition of the Al-SBA-15 supports and corresponding supported

291   NiO catalysts prepared with various Si/Al mole ratios were investigated using XRF elemental

292   analysis (**Table 1**). The calculated Ni content was in good agreement with the theoretical

293   value, verifying the effectiveness of wet impregnation for incorporating an accurate loading

294   of NiO onto the catalyst support. The experimental Si/Al molar ratio of the parent Al-SBA-

295   15 supports showed good agreement with the intended ratios (5, 25, 50 and 75), and within

296   the accuracy of the measurement was unchanged following doping with NiO.

297   The acidity of the synthesized catalysts was evaluated by temperature programmed

298   reaction of chemisorbed propylamine and TG-MS [44–46]. The peak intensity of the

299   desorption of the reactively formed propene is proportional to the acid site loading, while the

300   desorption temperature reflects the acid strength. **Figure S4** shows the temperature-

301   programmed desorption of reactively formed propene from propylamine decomposition over

302   the parent Al-SBA-15 supports, which indicates that the acidity of all synthesized materials

303   was greatly improved when Al^{3+} was present in the framework of the catalyst support. The

304   presence of NiO particles on the corresponding catalyst support (**Figure 3**) also slightly

305   increased the acid site loading slightly as shown in **Table 1,** which suggests Lewis acidic

306   Ni^{2+} sites in the surface of NiO may also contribute to propylamine decomposition. All

307   synthesized catalyst supports exhibited propene desorption in a similar range of temperatures

308   at ~430 °C, with the acid site loading increasing with decreased Si/Al molar ratio;

309   corresponding supported NiO catalyst exhibited a similar trend but with a slightly lower

310   desorption temperature of ~420 °C. The lower temperature of propene desorption suggests

311 there is a synergy between NiO and acid sites on the Al-SBA-15 support catalyst that

312 increases the acid strength of the synthesized catalyst. The most acidic catalyst is Ni/Al-SBA-

313 15(5), which is believed to comprise a large amount of both Brønsted and Lewis acidic sites.

314 The lowest acid site loading was observed for Ni-SBA-15, which had only Lewis acid sites,

315 and is most likely attributed to defects on the SiO_2 support and low coordination Ni^{2+} sites in

316 the surface of NiO nanoparticles. The effect of Brønsted and Lewis acidic sites on the catalyst

317 acidity can be observed in **Figure 4**, which shows the DRIFT spectra of chemisorbed pyridine

318 on the NiO/Al-SBA-15 and NiO/SBA-15 catalysts. The absorption bands at approximately

319 1446, 1570 and 1590-1600 cm^{-1} correspond to pyridine adsorption at the Lewis acid sites

320 [45]. The Brønsted acid sites arise from the pyridine adsorption band at approximately 1547

321 and 1640 cm^{-1}, while the 1490 cm^{-1} band is attributed to pyridine adsorbed at the Brønsted

322 and Lewis acid sites [44]. The bands at 1446 and 1590 cm^{-1} may also have a contribution

323 from pyridine hydrogen bonded to weak silanol groups [44,47]. As the Si/Al molar ratio

324 decreases the intensity of bands at 1547 cm^{-1} and 1640 cm^{-1} and 1490 cm^{-1} increases,

325 indicative of the genesis of Brønsted acid sites in the Si-O-Al framework, while the intensity

326 of the Lewis acid bands remained almost unchanged. The intensity of the band associated

327 with the Brønsted acid increased proportionally with an decreased Si/Al molar ratio (i.e. Al^{3+}

328 content). The absence of Brønsted acid bands in NiO/SBA-15 further evidences that Brønsted

329 acidity arises in the aforementioned catalysts from Si-O-Al interactions, and that some Lewis

330 acidity originates from Ni^{2+} in NiO [32].

331 The distribution of Al^{3+} in Al-SBA-15 and corresponding NiO-supported catalyst can

332 be elucidated by ^{27}Al and ^{29}Si MAS NMR of the parent support and for NiO/Al-SBA-15(5)

333 (**Figure 5**), with ^{27}Al MAS NMR spectra distinguishing between framework and extra-

334   framework Al^{3+} species in SBA-15. The interaction of Al^{3+} with the SBA-15 catalyst support

335   results in three resolved peaks arising in the NMR spectrum at chemical shifts of

336   approximately 51, 27 and 0 ppm. The peak line at approximately 51 ppm demonstrates the

337   incorporation of Al^{3+} species into the SBA-15 framework via tetrahedral coordination (AlO_4

338   structural unit, Al(tet)) of Al^{3+} covalently bound to four Si atoms via oxygen bridges [48,49].

339   Meanwhile, the peaks at approximately 27 and 0 ppm are assigned to the non-framework or

340   extra-framework coordination of Al^{3+} as pentahedral (AlO_5 structure unit, Al(penta)) and

341   octahedral (AlO_6 structure unit, Al(oct)) arrangements [50,51]. The Al-SBA-15(5) shows the

342   simultaneous presence of all three peaks for AlO_4, AlO_5 and AlO_6 structural units, which

343   suggests at high Al content more Al was present in an extra-framework form [48,52]. As the

344   Al content is decreased to Al-SBA-15(50) and Al-SBA-15(75), the tetrahedral peak at 51

345   ppm is dominant indicating the successful incorporation of just framework Al^{3+} into SBA-

346   15. The TLCT thus method proved successful in doping the walls of SBA-15 by the

347   incorporation of Al^{3+} species into the SBA-15 framework without destroying the SBA-15

348   structure. For NiO/Al-SBA-15(5) the peaks associated with pentahedral (27 ppm) and

349   octahedral (0 ppm) Al^{3+} decrease significantly compared to the parent Al-SBA-15(5). This

350   suggests that highly reactive extra-framework Al-OH groups in the parent support may have

351   interacted with Ni^{2+}, thereby altering the coordination of extra-framework Al^{3+}. Such

352   interactions in NiO/Al-SBA-15(5), coupled with paramagnetic effects from NiO may

353   account for the decreased intensity of pentahedral (27 ppm) and octahedral (0 ppm) peaks

354   observed in **Figure 5a** [38,53,54]. In contrast, the framework Al^{3+} species at 51 ppm is

355   relatively unchanged upon doping with NiO indicating the stability of this species during the

356   impregnation step. The ^{29}Si MAS NMR spectra of Al-SBA-15 and NiO/Al-SBA-15(5) shows

357 a relatively broad, featureless band at about -109 ppm. The chemical shift range for ^{29}Si for

358 aluminosilicates is relatively narrow spanning -102 to -116 ppm, with Si (3 Si, 1 A1) expected

359 around -106 ppm [ref]. Thus the peak observed for Al-SBA-15 falls in the correct range for

360 $Si(O-Si)_n(OAl)_{4-n}$ units, with the broadness of the peak reflecting the amorphous nature of

361 the mesoporous walls of Al-SBA-15 [55,56]. The strong interaction of paramagnetic NiO

362 with the Al-SBA-15 catalyst support reduces the intensity of the ^{29}Si signal from NiO/Al-

363 SBA-15(5) relative to the Al-SBA-15(5) parent support [54].

364   The morphological characteristics of Al-SBA-15(5), NiO/Al-SBA-15(5) and

365 NiO/SBA-15 were further explored by HRTEM as shown in **Figure 6**. **Figure 6a** shows the

366 well-defined mesoporous channels of Al-SBA-15(5) are not significantly different to that of

367 SBA-15 the structure shown in **Figure 6b** owing to the ease of incorporation of Al^{3+} into the

368 mesoporous framework [28]. **Figure 6c** shows the mesopores are retained in NiO/Al-SBA-

369 15(5) upon NiO doping, with NiO particles well dispersed throughout the pore network. The

370 uniform pore size distribution of the mesoporous Al-SBA-15 support catalyst can limit the

371 agglomeration and particle growth of NiO, ensuring a good dispersion of small NiO

372 nanoparticles in the resulting NiO/Al-SBA-15(5) catalyst [24], [38]. **Figure 6b** and **c** also

373 shows NiO/Al-SBA-15(5) has a higher NiO dispersion than NiO-SBA-15, suggesting a

374 stronger interaction of NiO with Al-SBA-15(5) reduces sintering. Further analysis by

375 HRTEM-EDS chemical mapping in **Figure S5** verifies that some NiO agglomeration

376 occurred over SBA-15 supports. For NiO/Al-SBA-15 a homogenous distribution of Si, O, Al

377 and Ni is observed, further confirming the uniform dispersion of NiO and within the Al-SBA-

378 15 framework. The use of media with the appropriate water/ethanol ratio in the wet

379 impregnation method correspondingly increases the NiO dispersion, as the mixed solvent

380 increases the diffusion rate of the Ni salt precursor and the adhesion of the NiO to the

381 mesoporous structure of the catalyst support [30,57]. Finally, the EDS chemical mapping

382 analysis also supports the XRF elemental analysis, with the close nominal value of the Ni

383 content and Si/Al molar ratio employed in catalyst synthesis.

384

385 **3.2 Deoxygenation activity of PFAD**

386 The catalytic activity of NiO-SBA-15 and NiO/Al-SBA-15 catalysts with different

387 Si/Al molar ratios of 5-75 was studied in the solventless DO reaction of PFAD under a

388 nitrogen gas atmosphere. The reaction was conducted in a semi-batch reactor with 5 wt%

389 catalyst loading at 350 °C for 2 hours. A blank experiment was carried out in the absence of

390 catalyst under the same reaction conditions to determine the product distribution during the

391 thermal decomposition of PFAD. **Figure 7** reveals all NiO/Al-SBA-15 and NiO/SBA-15 are

392 active for the conversion of PFAD, producing a high yield (81-86%) of saturated and

393 unsaturated straight-chain hydrocarbons, with a selectivity towards the diesel range n-(C_{11}-

394 C_{17}) fraction spanning 81-91%. In the absence of catalyst thermal cracking of PFAD

395 produces only a 22% yield of hydrocarbons with a higher 56.8% selectivity towards gasoline

396 range n-(C_8-C_{10}) products observed.

397 An effective catalyst for DO should remove oxygen from FFA while avoiding carbon

398 loss from C-C cracking to form light straight chain hydrocarbons. The product selectivity for

399 n-(C_8-C_{17}) deoxygenated products are shown **Figure S6**, while **Figure 8** summarises

400 fractions groups together over the ranges C_{8-10}, C_{11-14} and C_{15-17}. In the absence of catalyst the

401 majority of hydrocarbon products lie in the n-C_8 and n-C_9 fractions due to cracking being the

402 dominant process, while over NiO/Al-SBA-15 or NiO/SBA-15, n-C_{15} and n-C_{17} products are

403   favoured. These fractions are largely associated with the FFA composition in PFAD, which

404   comprises ~47% of C_{16} (palmitic acid), ~51% of C_{18} (steric acid, oleic acid, linoleic acid and

405   linolenic acid) and 1-2% of FFAs with carbon numbers C_{12} and C_{14}. DO reaction proceeds

406   via decarboxylation (eq 1), decarbonylation (eq 2) and cracking (eq 3-4) [39], thus the desired

407   pathway must be controlled to attain a high selectivity of the hydrocarbon product. The high

408   selectivity towards n-C_{15} and n-C_{17} suggests DCX/DCN reaction pathways are favoured

409   which reduces the carbon chain length by one unit upon removal of CO_2 or CO respectively.

410

411   *Decarboxylation (DCX) of FFA*

412            $RCOOH \longrightarrow CO_2 + RH$ (1)

413

414   *Decarbonylation (DCN) of FFA*

415            $RCOOH \longrightarrow CO + H_2O + RH$ (2)

416

417   *Cracking*

418            $R_x - R_y \longrightarrow R_x = CH + R_y = CH$ (3)

419            $R_x COOH \longrightarrow R_{x-1}H + R_x COOH$ (4)

420

421   **Figure 9** shows the distribution of unsaturated and saturated n-C_{15} products comprises >85%

422   of straight-chain alkanes, suggesting DCX was the dominant reaction pathway. The high

423   dispersion of NiO on Al-SBA-15 and SBA-15 is most likely responsible for the improved

424   hydrocarbon yield and high diesel selectivity during DO of PFAD. Hydrocarbon cracking

425   via C-C scission of deoxygenated n-C_{15} and n-C_{17} chains (eq 3) or long-chain C_{16} and C_{18}

426   FFAs (eq 4) can produce n-(C_8-C_{16}) hydrocarbons, and are both favoured by high reaction

427   temperatures or the presence of strongly acidic sites. The slight increase in selectivity towards

428   the n-C_{15} fraction from NiO/SBA-15 to mildly acidic NiO/Al-SBA-15(50 and 75) (**Figure**

429   **S6**) may reflect the improved NiO dispersion over these catalysts. In contrast the slight

430   decrease in selectivity towards n-C_{15} and n-C_{17} and increase in shorter chain n-C_{8-10} and n-

431   C_{11-14} fractions (**Figure 8**) over NiO/Al-SBA-15(25 and 5) may reflect their slightly

432   increased acidity which may increase C-C cracking [32,55]. Future work will explore the

433   kinetics of DCN, DCX and cracking of model FFA substrates to further assess the impact of

434   acidity on green-diesel product selectivity.

435

436

437   **4. CONCLUSIONS**

438   A series of templated mesoporous Al-SBA-15 supports with Si/Al molar ratios

439   spanning 5-75 were successfully synthesised by a true liquid crystal templating (TLCT)

440   method. Subsequent wet impregnation with $Ni(NO_3)_2.6H_2O$ from an ethanolic solution was

441   used to produce NiO/Al-SBA-15 catalysts, with well-dispersed 9-10 nm NiO nanoparticle

442   sizes. Acid site loadings determined from temperature programmed reaction of propylamine

443   reveal the acid site loading increases with decreased Si:Al ratio, while ^{27}Al and ^{29}Si MAS-

444   NMR demonstrated that framework Al^{3+} was stable towards NiO functionalisation. NiO/Al-

445   SBA-15 and NiO/SBA-15 catalysts all exhibit excellent catalytic activity for PFAD

446   deoxygenation producing hydrocarbon yields of 81-86% and a selectivity to the diesel

447   fraction (C_{11}-C_{17}) of 81-91%. In the absence of catalyst, thermal cracking of PFAD is the

448   dominant process, whereas for supported NiO catalysts deoxygenation proceeds mainly via

449 DCX and DCN processes, with the DCX:DCN ratio for the main n-C$_{15}$ fraction found to

450 increase with decreased Si:Al ratio in the support. Low Si/Al molar ratios led to a slight

451 decrease in selectivity towards diesel range (C$_{11}$-C$_{20}$) hydrocarbons which may be attributed

452 to the increased acid loading favouring cracking reactions.

453

461

462

463

464

465

466

471

472   **REFERENCES**

473   [1]   A.A. Mancio, S.A.P. da Mota, C.C. Ferreira, T.U.S. Carvalho, O.S. Neto, J.R. Zamian,

474   M.E. Araújo, L.E.P. Borges, N.T. Machado, Separation and characterization of

475   biofuels in the jet fuel and diesel fuel ranges by fractional distillation of organic liquid

476   products, Fuel. 215 (2018) 212–225. doi:10.1016/j.fuel.2017.11.029.

477   [2]   L.M. Orozco, D.A. Echeverri, L. Sï¿½nchez, L.A. Rios, Second-generation green

478   diesel from castor oil: Development of a new and efficient continuous-production

479   process, Chem. Eng. J. 322 (2017) 149–156. doi:10.1016/j.cej.2017.04.027.

480   [3]   S.B. Glisic, J.M. Pajnik, A.M. Orlović, Process and techno-economic analysis of green

481   diesel production from waste vegetable oil and the comparison with ester type

482   biodiesel production, Appl. Energy. 170 (2016) 176–185.

483   doi:10.1016/j.apenergy.2016.02.102.

484   [4]   M.F. Othman, A. Adam, G. Najafi, R. Mamat, Green fuel as alternative fuel for diesel

485   engine: A review, Renew. Sustain. Energy Rev. 80 (2017) 694–709.

486   doi:10.1016/j.rser.2017.05.140.

487   [5]   C. Perego, A. Bosetti, Biomass to fuels: The role of zeolite and mesoporous materials,

488   Microporous Mesoporous Mater. 144 (2011) 28–39.

489   doi:10.1016/j.micromeso.2010.11.034.

490   [6]   A. Srifa, K. Faungnawakij, V. Itthibenchapong, S. Assabumrungrat, Roles of

491   monometallic catalysts in hydrodeoxygenation of palm oil to green diesel, Chem. Eng.

492   J. 278 (2015) 249–258. doi:10.1016/j.cej.2014.09.106.

493   [7]   A. Srifa, R. Kaewmeesri, C. Fang, V. Itthibenchapong, K. Faungnawakij, NiAl 2 O 4

494   spinel-type catalysts for deoxygenation of palm oil to green diesel, Chem. Eng. J. 345

495   (2018) 107–113. doi:10.1016/j.cej.2018.03.118.

496   [8]   A. Gapor Md Top, Production and utilization of palm fatty acid distillate (PFAD),

497   Lipid Technol. 22 (2010) 11–13. doi:10.1002/lite.200900070.

498   [9]   B. Tay, Y. Ping, M. Yusof, Characteristics and Properties of Fatty Acid Distillates

499   from Palm Oil, 59 (2009) 5–11.

500   [10]   I.M. Lokman, M. Goto, U. Rashid, Y.H. Taufiq-Yap, Sub- and supercritical

501   esterification of palm fatty acid distillate with carbohydrate-derived solid acid catalyst,

502   Chem. Eng. J. 284 (2016) 872–878. doi:10.1016/j.cej.2015.08.102.

503   [11]   G.A. Alsultan, N. Asikin-mijan, H. V Lee, A.S. Albazzaz, Deoxygenation of waste

504   cooking to renewable diesel over walnut shell- derived nanorode activated carbon

505   supported CaO-La 2 O 3 catalyst, Energy Convers. Manag. 151 (2017) 311–323.

506   doi:10.1016/j.enconman.2017.09.001.

507   [12]   K. Jeništová, I. Hachemi, P. Mäki-Arvela, N. Kumar, M. Peurla, L. Čapek, J. Wärnå,

508   D.Y. Murzin, Hydrodeoxygenation of stearic acid and tall oil fatty acids over Ni-

509   alumina catalysts: Influence of reaction parameters and kinetic modelling, Chem. Eng.

510   J. 316 (2017) 401–409. doi:10.1016/j.cej.2017.01.117.

511   [13]   C. Miao, O. Marin-Flores, S.D. Davidson, T. Li, T. Dong, D. Gao, Y. Wang, M.

512   Garcia-Pérez, S. Chen, Hydrothermal catalytic deoxygenation of palmitic acid over

513   nickel catalyst, Fuel. 166 (2016) 302–308. doi:10.1016/j.fuel.2015.10.120.

514 [14] E. Santillan-Jimenez, M. Crocker, Catalytic deoxygenation of fatty acids and their

515 derivatives to hydrocarbon fuels via decarboxylation/decarbonylation, J. Chem.

516 Technol. Biotechnol. 87 (2012) 1041–1050. doi:10.1002/jctb.3775.

517 [15] B.P. Pattanaik, R.D. Misra, Effect of reaction pathway and operating parameters on

518 the deoxygenation of vegetable oils to produce diesel range hydrocarbon fuels: A

519 review, Renew. Sustain. Energy Rev. 73 (2017) 545–557.

520 doi:10.1016/j.rser.2017.01.018.

521 [16] N. Arun, R. V. Sharma, A.K. Dalai, Green diesel synthesis by hydrodeoxygenation of

522 bio-based feedstocks: Strategies for catalyst design and development, Renew. Sustain.

523 Energy Rev. 48 (2015) 240–255. doi:10.1016/j.rser.2015.03.074.

524 [17] B.M. Murphy, B. Xu, Foundational techniques for catalyst design in the upgrading of

525 biomass-derived multifunctional molecules, Prog. Energy Combust. Sci. 67 (2018)

526 1339–1351. doi:10.1016/j.pecs.2018.01.003.

527 [18] C. Kordulis, K. Bourikas, M. Gousi, E. Kordouli, A. Lycourghiotis, Development of

528 nickel based catalysts for the transformation of natural triglycerides and related

529 compounds into green diesel: A critical review, Appl. Catal. B Environ. 181 (2016)

530 156–196. doi:10.1016/j.apcatb.2015.07.042.

531 [19] P. Kumar, S.R. Yenumala, S.K. Maity, D. Shee, Kinetics of hydrodeoxygenation of

532 stearic acid using supported nickel catalysts: Effects of supports, Appl. Catal. A Gen.

533 471 (2014) 28–38. doi:10.1016/j.apcata.2013.11.021.

534 [20] P.T. Huyen, L.T.H. Nam, T.Q. Vinh, C. Mart??nez, V.I. Parvulescu, ZSM-5/SBA-15

535 versus Al-SBA-15 as supports for the hydrocracking/hydroisomerization of alkanes,

536 Catal. Today. (2016). doi:10.1016/j.cattod.2017.03.040.

537   [21]   P. Bhanja, A. Bhaumik, Porous nanomaterials as green catalyst for the conversion of

538   biomass to bioenergy, Fuel. 185 (2016) 432–441. doi:10.1016/j.fuel.2016.08.004.

539   [22]   W. Li, D. Zhao, An overview of the synthesis of ordered mesoporous materials.,

540   Chem. Commun. (Camb). 49 (2013) 943–6. doi:10.1039/c2cc36964h.

541   [23]   C.M.A. Parlett, K. Wilson, A.F. Lee, Hierarchical porous materials: catalytic

542   applications, Chem. Soc. Rev. 42 (2013) 3876–3893. doi:10.1039/C2CS35378D.

543   [24]   S.G. Wainwright, C.M.A. Parlett, R.A. Blackley, W. Zhou, A.F. Lee, K. Wilson, D.W.

544   Bruce, True liquid crystal templating of SBA-15 with reduced microporosity,

545   Microporous Mesoporous Mater. 172 (2013) 112–117.

546   doi:10.1016/j.micromeso.2013.01.016.

547   [25]   I. Tyrone Ghampson, C. Sepúlveda, R. Garcia, J.L. García Fierro, N. Escalona, W.J.

548   Desisto, Comparison of alumina- and SBA-15-supported molybdenum nitride

549   catalysts for hydrodeoxygenation of guaiacol, Appl. Catal. A Gen. 435–436 (2012)

550   51–60. doi:10.1016/j.apcata.2012.05.039.

551   [26]   N. Rahmat, A.Z. Abdullah, A.R. Mohamed, A Review : Mesoporous Santa Barbara

552   Amorphous-15 , Types , Synthesis and Its Applications towards Biorefinery

553   Production Norhasyimi Rahmat , 2 Ahmad Zuhairi Abdullah , 2 Abdul Rahman

554   Mohamed Faculty of Chemical Engineering , University Technology MARA , S, Am.

555   J. Appl. Sci. 7 (2010) 1579–1586. doi:10.3844/ajassp.2010.1579.1586.

556   [27]   R. Nisticò, D. Scalarone, G. Magnacca, Sol-gel chemistry, templating and spin-

557   coating deposition: A combined approach to control in a simple way the porosity of

558   inorganic thin films/coatings, Microporous Mesoporous Mater. 248 (2017) 18–29.

559   doi:10.1016/j.micromeso.2017.04.017.

560 [28] S. Gbadamasi, H. Ali, H. Voon, Y. Atta, P. Sudarsanam, K. Bhargava, B. Abd Hamid,

561 Promising Ni/Al-SBA-15 catalysts for hydrodeoxygenation of dibenzofuran into fuel

562 grade hydrocarbons: synergetic effect of Ni and Al-SBA-15 support, RSC Adv. 6

563 (2016) 25992–26002. doi:10.1039/C5RA27526A.

564 [29] Y. Yue, A. Gédéon, J.-L. Bonardet, N. Melosh, J.-B. D 'espinose, J. Fraissard, Direct

565 synthesis of AlSBA mesoporous molecular sieves: characterization and catalytic

566 activities, Chem.Commun. (1999) 1967–1968. doi:10.1039/a904467a.

567 [30] A.K. Medina-Mendoza, M.A. Cortés-Jácome, J.A. Toledo-Antonio, C. Angeles-

568 Chávez, E. López-Salinas, I. Cuauhtémoc-López, M.C. Barrera, J. Escobar, J.

569 Navarrete, I. Hernández, Highly dispersed uniformly sized Pt nanoparticles on

570 mesoporous Al-SBA-15 by solid state impregnation, Appl. Catal. B Environ. 106

571 (2011) 14–25. doi:10.1016/j.apcatb.2011.04.031.

572 [31] P.T. Huyen, L.T.H. Nam, T.Q. Vinh, C. Martínez, V.I. Parvulescu, ZSM-5/SBA-15

573 versus Al-SBA-15 as supports for the hydrocracking/hydroisomerization of alkanes,

574 Catal. Today. 306 (2018) 121–127. doi:10.1016/j.cattod.2017.03.040.

575 [32] N. Asikin-Mijan, H.V. Lee, J.C. Juan, A.R. Noorsaadah, Y.H. Taufiq-Yap, Catalytic

576 deoxygenation of triglycerides to green diesel over modified CaO-based catalysts,

577 RSC Adv. 7 (2017) 46445–46460. doi:10.1039/C7RA08061A.

578 [33] D.P. Gamliel, B.P. Baillie, E. Augustine, J. Hall, G.M. Bollas, J.A. Valla, Nickel

579 impregnated mesoporous USY zeolites for hydrodeoxygenation of anisole,

580 Microporous Mesoporous Mater. 261 (2018) 18–28.

581 doi:10.1016/j.micromeso.2017.10.027.

582 [34] N. Asikin-Mijan, H. V. Lee, G. Abdulkareem-Alsultan, A. Afandi, Y.H. Taufiq-Yap,

583   Production of green diesel via cleaner catalytic deoxygenation of Jatropha curcas oil,

584   J. Clean. Prod. 167 (2018) 1048–1059. doi:10.1016/j.jclepro.2016.10.023.

585 [35] C.M.A. Parlett, A. Aydin, L.J. Durndell, L. Frattini, M.A. Isaacs, A.F. Lee, X. Liu, L.

586   Olivi, R. Trofimovaite, K. Wilson, C. Wu, Tailored mesoporous silica supports for Ni

587   catalysed hydrogen production from ethanol steam reforming, Catal. Commun. 91

588   (2017) 76–79. doi:10.1016/j.catcom.2016.12.021.

589 [36] Y. Yang, G. Lv, L. Deng, B. Lu, J. Li, J. Zhang, J. Shi, S. Du, Renewable aromatic

590   production through hydrodeoxygenation of model bio-oil over mesoporous Ni/SBA-

591   15 and Co/SBA-15, Microporous Mesoporous Mater. 250 (2017) 47–54.

592   doi:10.1016/j.micromeso.2017.05.022.

593 [37] N. Asikin-Mijan, H. V. Lee, T.S. Marliza, Y.H. Taufiq-Yap, Pyrolytic-deoxygenation

594   of triglycerides model compound and non-edible oil to hydrocarbons over SiO2-

595   Al2O3 supported NiO-CaO catalysts, J. Anal. Appl. Pyrolysis. 129 (2017) 221–230.

596   doi:10.1016/j.jaap.2017.11.009.

597 [38] Y. Li, D. Pan, C. Yu, Y. Fan, X. Bao, Synthesis and hydrodesulfurization properties

598   of NiW catalyst supported on high-aluminum-content, highly ordered, and

599   hydrothermally stable Al-SBA-15, J. Catal. 286 (2012) 124–136.

600   doi:10.1016/j.jcat.2011.10.023.

601 [39] S. Zulkepli, J.C. Juan, H.V. Lee, N.S.A. Rahman, P.L. Show, E.P. Ng, Modified

602   mesoporous HMS supported Ni for deoxygenation of triolein into hydrocarbon-

603   biofuel production, Energy Convers. Manag. 165 (2018) 495–508.

604   doi:10.1016/j.enconman.2018.03.087.

605 [40] S.M. Morris, P.F. Fulvio, M. Jaroniec, Ordered Mesoporous Alumina-Supported

606   Metal Oxides Ordered Mesoporous Alumina-Supported Metal Oxides, October. 130

607   (2008) 15210–15216. doi:10.1021/ja806429q.

608 [41] D. Zhao, J. Sun, Q. Li, G.D. Stucky, S. Barbara, Morphological Control of Highly

609   Ordered Mesoporous Silica SBA-15 Mesoporous materials are of great interest to the

610   materials community because their pore structures as well as catalytic , adsorbed ,

611   conductive and magnetic ordered large mesoporous silica , Communications. 12

612   (2000) 275–279. doi:10.1021/cm9911363.

613 [42] J.C. Groen, L.A.A. Peffer, J. Pérez-Ramírez, Pore size determination in modified

614   micro- and mesoporous materials. Pitfalls and limitations in gas adsorption data

615   analysis, Microporous Mesoporous Mater. 60 (2003) 1–17. doi:10.1016/S1387-

616   1811(03)00339-1.

617 [43] K. Soni, K.C. Mouli, A.K. Dalai, J. Adjaye, Influence of frame connectivity of SBA-

618   15 and KIT-6 supported NiMo catalysts for hydrotreating of gas oil, Catal. Letters.

619   136 (2010) 116–125. doi:10.1007/s10562-010-0317-0.

620 [44] A. Berenguer, J.A. Bennett, J. Hunns, I. Moreno, J.M. Coronado, A.F. Lee, P. Pizarro,

621   K. Wilson, D.P. Serrano, Catalytic hydrodeoxygenation of m-cresol over

622   Ni2P/hierarchical ZSM-5, Catal. Today. 304 (2017) 72–79.

623   doi:10.1016/j.cattod.2017.08.032.

624 [45] Z. Tai, M.A. Isaacs, C.M.A. Parlett, A.F. Lee, K. Wilson, High activity magnetic core-

625   mesoporous shell sulfonic acid silica nanoparticles for carboxylic acid esterification,

626   Catal. Commun. Commun. 92 (2017) 56–60. doi:10.1016/j.catcom.2017.01.004.

627 [46] C. Pirez, K. Wilson, A.F. Lee, An energy-efficient route to the rapid synthesis of

628   organically-modified SBA-15 via ultrasonic template removal, Green Chem. 16

629   (2014) 197–202. doi:10.1039/C3GC40474A.

630   [47]   J.C. Manayil, A. Osatiashtiani, A. Mendoza, C.M.A. Parlett, M.A. Isaacs, L.J.

631   Durndell, C. Michailof, E. Heracleous, A. Lappas, A.F. Lee, K. Wilson, Impact of

632   Macroporosity on Catalytic Upgrading of Fast Pyrolysis Bio-Oil by Esterification over

633   Silica Sulfonic Acids, ChemSusChem. 10 (2017) 3506–3511.

634   doi:10.1002/cssc.201700959.

635   [48]   N. Lin, J.Y. Yang, Z.Y. Wu, H.J. Wang, J.H. Zhu, Tailoring the Al-distribution and

636   performance of mesoporous silica SBA-15 through one-pot synthesis, Microporous

637   Mesoporous Mater. 139 (2011) 130–137. doi:10.1016/j.micromeso.2010.10.029.

638   [49]   Z. Luan, M. Hartmann, D. Zhao, W. Zhou, L. Kevan, Alumination and Ion Exchange

639   of Mesoporous SBA-15 Molecular Sieves, Chem. Mater. 11 (1999) 1621–1627.

640   doi:10.1021/cm9900756.

641   [50]   A.J.J. Koekkoek, J.A.R. Van Veen, P.B. Gerrtisen, P. Giltay, P.C.M.M. Magusin,

642   E.J.M. Hensen, Brønsted acidity of Al/SBA-15, Microporous Mesoporous Mater. 151

643   (2012) 34–43. doi:10.1016/j.micromeso.2011.11.019.

644   [51]   X. Wang, P. Du, K. Chi, A. Duan, C. Xu, Z. Zhao, Z. Chen, H. Zhang, Synthesis of

645   NiMo catalysts supported on mesoporous silica FDU-12 with different morphologies

646   and their catalytic performance of DBT HDS, Catal. Today. 291 (2017) 146–152.

647   doi:10.1016/j.cattod.2016.10.035.

648   [52]   S. Zeng, J. Blanchard, M. Breysse, Y. Shi, X. Shu, H. Nie, D. Li, Post-synthesis

649   alumination of SBA-15 in aqueous solution: A versatile tool for the preparation of

650   acidic Al-SBA-15 supports, Microporous Mesoporous Mater. 85 (2005) 297–304.

651   doi:10.1016/j.micromeso.2005.06.031.

652 [53] A. Sampieri, S. Pronier, S. Brunet, X. Carrier, C. Louis, J. Blanchard, K. Fajerwerg,

653   M. Breysse, Formation of heteropolymolybdates during the preparation of Mo and

654   NiMo HDS catalysts supported on SBA-15: Influence on the dispersion of the active

655   phase and on the HDS activity, Microporous Mesoporous Mater. 130 (2010) 130–141.

656   doi:10.1016/j.micromeso.2009.10.024.

657 [54] C.R. Patil, C. V. Rode, Synthesis of diesel additives from fructose over PWA/SBA-

658   15 catalyst, Fuel. 217 (2018) 38–44. doi:10.1016/j.fuel.2017.12.027.

659 [55] W. Hu, Q. Luo, Y. Su, L. Chen, Y. Yue, C. Ye, F. Deng, Acid sites in mesoporous Al-

660   SBA-15 material as revealed by solid-state NMR spectroscopy, Microporous

661   Mesoporous Mater. 92 (2006) 22–30. doi:10.1016/j.micromeso.2005.12.013.

662 [56] R.D. Andrei, M.I. Popa, F. Fajula, V. Hulea, Heterogeneous oligomerization of

663   ethylene over highly active and stable Ni-AlSBA-15 mesoporous catalysts, J. Catal.

664   323 (2015) 76–84. doi:10.1016/j.jcat.2014.12.027.

665 [57] M. Tao, X. Meng, Y. Lv, Z. Bian, Z. Xin, Effect of impregnation solvent on Ni

666   dispersion and catalytic properties of Ni/SBA-15 for CO methanation reaction, Fuel.

667   165 (2016) 289–297. doi:10.1016/j.fuel.2015.10.023.

668

669

670

671

672

673

674

FIGURE CAPTIONS

676 **Fig 1**. a) Low-angle and b) wide-angle XRD patterns for NiO-SBA-15 and various Si/Al

677 molar ratios for the NiO/Al-SBA-15 catalyst

678

679 **Fig 2**. a) N_2 adsorption-desorption isotherms and b) Pore size distribution of synthesized

680 NiO/Al-SBA-15 and NiO/SBA-15 catalysts.

681

682 **Fig 3**. Temperature-programmed desorption of reactively formed propene from propylamine

683 decomposition over NiO/Al-SBA-15 and NiO/SBA-15 catalysts.

684

685 **Fig 4**. DRIFT spectra of chemisorbed pyridine for NiO/Al-SBA-15 and NiO/SBA-15

686 catalysts.

687

688 **Fig 5.** a) ^{27}Al and b) ^{29}Si NMR MAS spectra of the Al-SBA-15 and SBA-15 catalyst supports

689 and Ni/Al- SBA-15(5) catalyst

690

691 **Fig 6.** HRTEM image of a) Al-SBA-15(5), b) NiO/SBA-15 and c) NiO/Al-SBA-15(5)

692

693 **Fig 7.** Hydrocarbon yield of deoxygenated liquid product with gasoline (C_8-C_{10}) and diesel

694 (C_{11}-C_{18}) distribution range using synthesized NiO/SBA-15 and NiO/Al-SBA-15 catalysts

695

696 **Fig 8**. Comparison of selectivity towards C_{15}-C_{17}, C_{11}-C_{14} and C_8-C_{10} and fractions formed

697 during DO of PFAD.

698

699   **Fig 9**. Comparison of n-alkane and n-alkene hydrocarbon yields within the n-C$_{15}$ fraction

700

701

702

703

704

705

706

707

708

709

710

711

712

713

714

715

716   **FIGURES**

717

718   **Fig 1.**
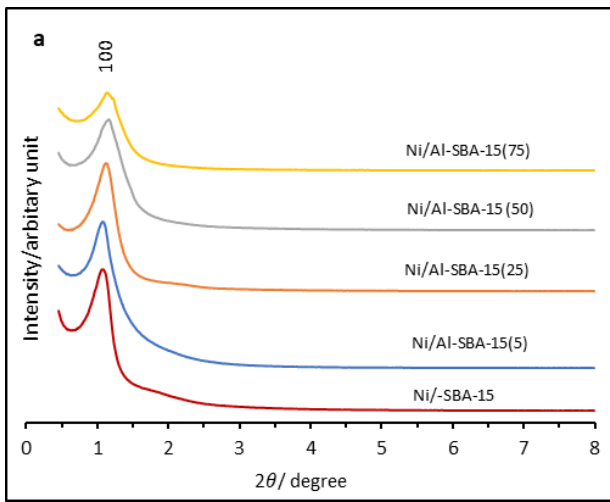
719
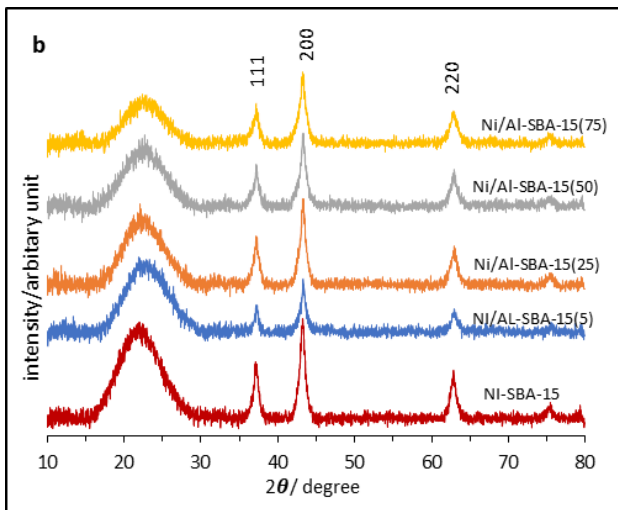
720

721

722

723

724

725

726

727

728

729 **Fig 2.**

730
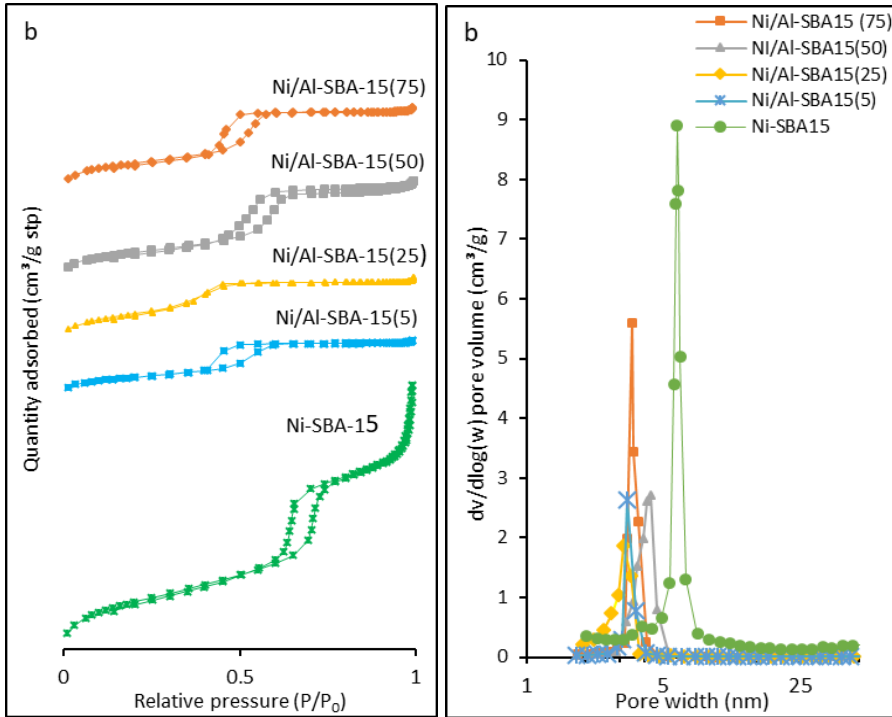
731

732

733

734

735

736

737

738

739

740

741

742   **Fig 3**.

743
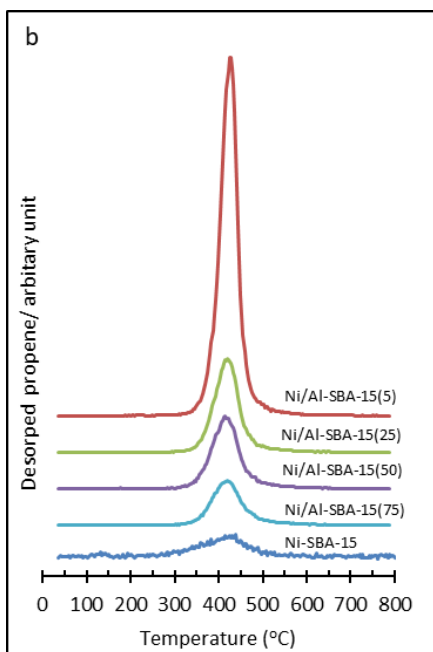
756   **Fig 4.**
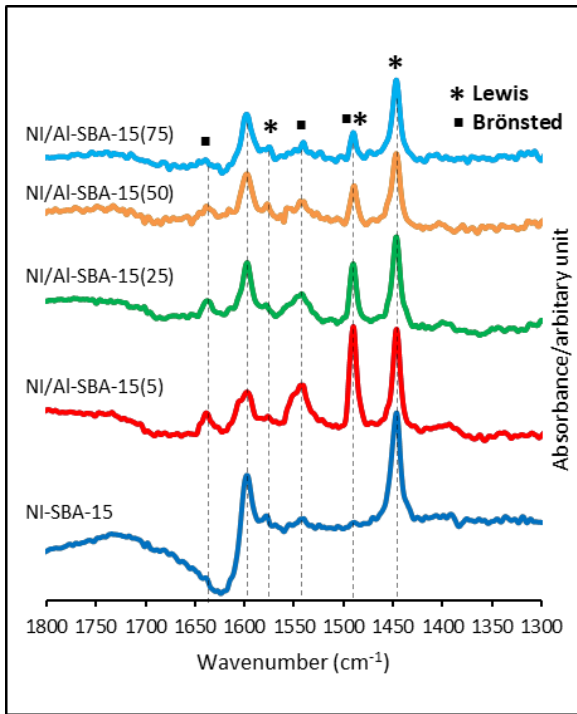
757

758

759   **Fig 5.**
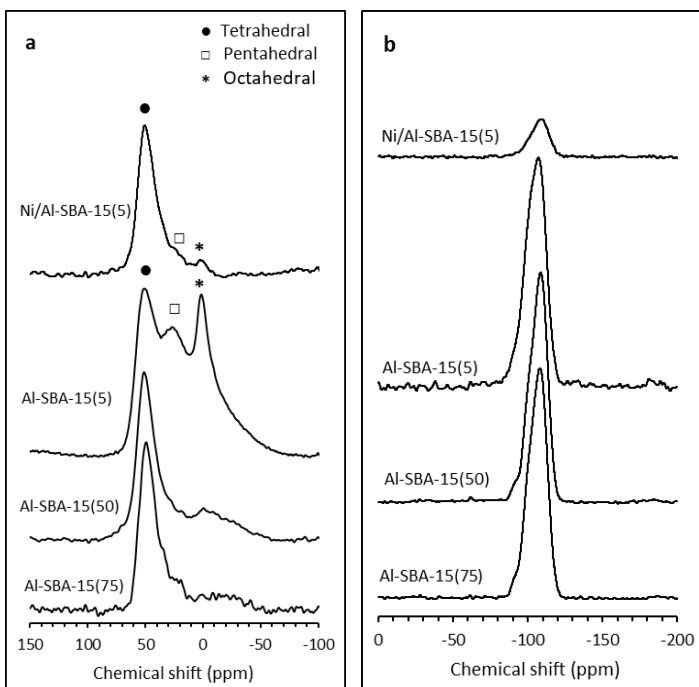
760

761   **Fig 6.**
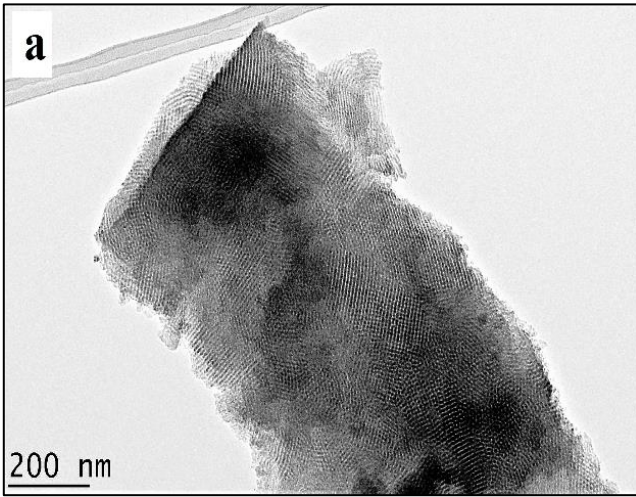
762
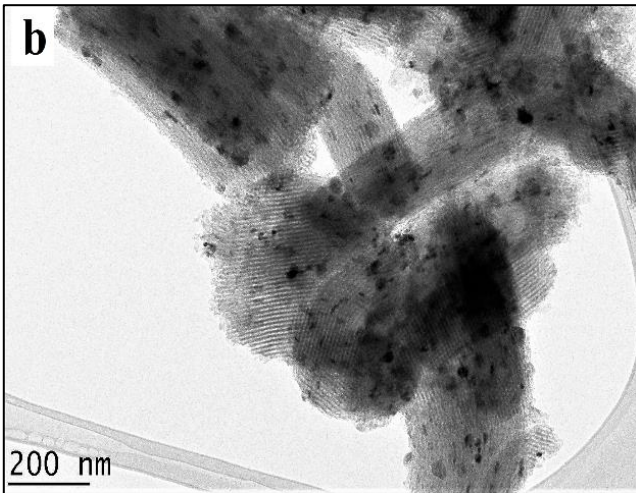
763
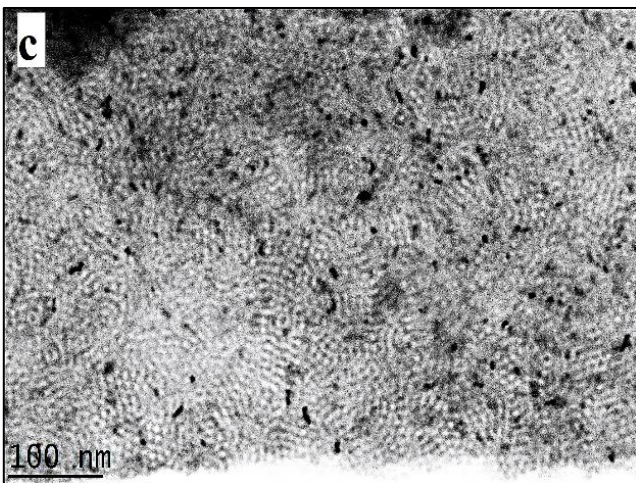
764

765 **Fig 7.**
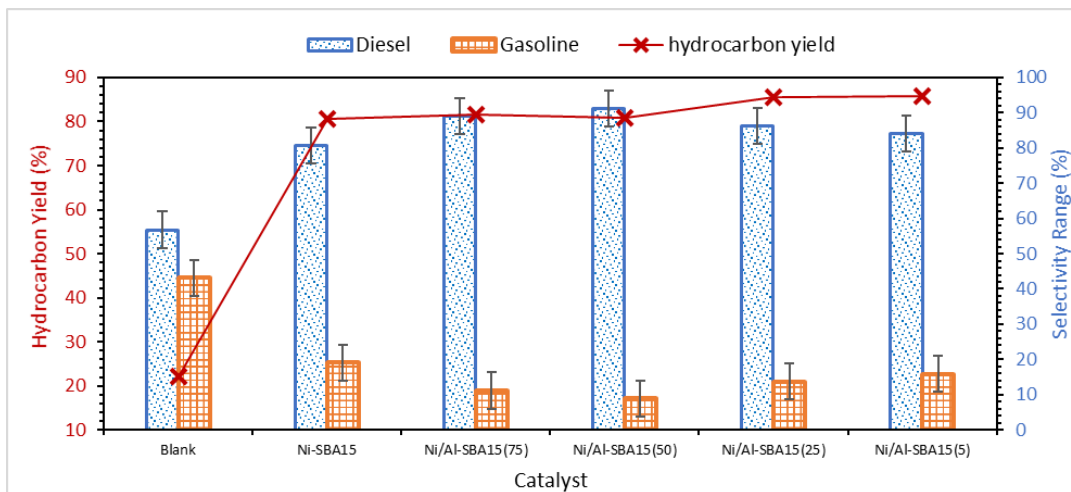
766

767

768

769

770

771 **Fig 8.**

772

773

774   **Fig 9.**

775